Tectonophysics 902 (2025) 230684

Contents lists available at ScienceDirect

Tectonophysics

journal homepage: www.elsevier.com/locate/tecto

Seismic imaging revealing the processes from subduction to arc-continental collision in the northeastern South China Sea

Xingyue Wang [a,b], Minghui Zhao [a,c,*], Xiaobo He [d], Jiazheng Zhang [a,c], Jinhui Cheng [a], Huabin Mao [b,e]

[a] Key Laboratory of Ocean and Marginal Sea Geology, South China Sea Institute of Oceanology, Chinese Academy of Sciences, Guangzhou, China
[b] Research Fleet, South China Sea Institute of Oceanology, Chinese Academy of Sciences, Guangzhou, China
[c] University of Chinese Academy of Sciences, Beijing, China
[d] Department of Ocean Exploration and Technology, Zhejiang Ocean University, Zhoushan, China
[e] State Key Laboratory of Tropical Oceanography, South China Sea Institute of Oceanology, Chinese Academy of Sciences, Guangzhou, China

ARTICLE INFO

Keywords:
Northeastern South China Sea
Velocity structure
Thinned continental crust
Low-velocity anomaly
Evolutionary model of subduction to collision

ABSTRACT

The northeastern margin of the South China Sea (SCS) is characterized by a tectonic shift from subduction in the south to arc-continent collision in the north. We describe the intraplate crustal-scale structure and deformation along a 256-km-long wide-angle reflection/refraction line perpendicular to the Manila Trench (MT). It is found that 1) the subducting plate of the northeast SCS comprises thinned continental crust with a thickness of 12–15 km and a high-velocity layer (HVL) with a thickness of 2–4 km, which is likely caused by (ultra)mafic intrusions; 2) the subducted upper crust is partly scraped off and accreted at the bottom of the accretionary wedge, and its characteristic low seismic-velocity may be due to subsequent hydration. Combined with previous investigations from six seismic lines in the study area across the MT and Southern Taiwan, from south to north, the velocity anomaly at the bottom of the accretionary wedge correspondingly undergoes a series of metamorphic processes in response to the transition from oceanic subduction to arc-continent collision.

1. Introduction

Since the Cenozoic, the South China Sea (SCS) has undergone a wide range of tectonic processes, including rifting-breakup, seafloor spreading, ridge jumps, and post-rift magmatic intrusion (Lester et al., 2014; Liu et al., 2021; Ren et al., 2002; Ru and Pigott, 1986; Sun et al., 2021; Wu et al., 2023; Zhao et al., 2010). The key features of the eastern boundary lie in the Taiwan arc-continent collision zone and the Manila Trench (MT) (Fig. 1). It is widely recognized that accretionary wedges are formed as a result of plate subduction, and their structure is determined by the various tectonic processes at the trench (Chiu et al., 2021; Dahlen, 1990; Tan et al., 2022). More specifically, a series of thrust faults within the accretionary wedge are widespread on the eastern side of the northern MT. Owing to the influence of the Taiwan arc-continent collision, the width and height of the accretionary wedge increased northward, accompanied by a significant change in shape (Lester et al., 2014; McIntosh et al., 2013; Tan et al., 2022). Previous studies on accretionary wedges are mainly based on Multi-Channel Seismic (MCS) profiles which reveal the geometry of internal faults (Gao et al., 2018; Wang et al., 2019; Zhu et al., 2017), but the internal seismic velocity structure of accretionary wedges has been rarely studied, which is the key to revealing the underlying tectonic processes.

The nature of the subduction slab in the northern Manila subduction zone has long been debated. Based on the magnetic data, Hsu et al. (2004) suggested that the area south of 21.5°N is oceanic crust, as evidenced by the magnetic anomaly strips. Regional seismic tomography has also favored the subduction of the oceanic crust (Amuru, 2007; Koulakov, 2011; Li et al., 2008), but the shallow (0–100 km) subduction slab features have barely been constrained due to limited resolution. In recent decades, many active-source seismic surveys have been conducted in the northeastern SCS (Fig. 1). These deep seismic survey lines revealed that subduction of thinned continental crust occurs north of ~20.2°N, whereas oceanic crust subduction occurs only south of it (Eakin et al., 2014; Liu et al., 2022; McIntosh et al., 2013). However, the tectonic processes for the transition from subduction to collision at the northeastern boundary of the SCS remain enigmatic.

* Corresponding author at: Key Laboratory of Ocean and Margin Sea Geology, South China Sea Institute of Oceanology, Chinese Academy of Sciences, Guangzhou 510301, China.
E-mail address: mhzhao@scsio.ac.cn (M. Zhao).

https://doi.org/10.1016/j.tecto.2025.230684
Received 11 November 2024; Received in revised form 27 February 2025; Accepted 1 March 2025
Available online 3 March 2025

More importantly, the structural changes of the accretionary wedge in the northern Manila subduction zone are significant for understanding the geological evolution process from subduction to collision and orogenic processes. Therefore, we aim to explore the seismic structure of the subducting plate and accretionary wedge in this area with wide-angle reflection/refraction seismic OBS data and MCS data along line Lx3 (Fig. 1) perpendicular to the MT in the northeastern SCS. Combined with previous results from other seismic lines in the study area, a tectonic evolution model of subduction to collision is proposed.

2. Geological setting

As one of the largest marginal seas in the western Pacific, the SCS is the product of internal tectonic processes and interactions among the Eurasian, Philippine, Pacific, and Indo-Australian plates. During the Cenozoic, the SCS was formed by a series of tectonic processes, including continental margin rifting, continental crust break-up, and seafloor spreading (Wu et al., 2023). In the early stage of SCS rifting, magmatic activity was weak, but very strong in the post-rift stage, accompanied by (ultra)mafic intrusions as evidenced by a widely distributed high-velocity layer (HVL) in the lower crust and volcanic activities in the northeastern SCS (Fan et al., 2017; Gao et al., 2015; Lester et al., 2014; Liu et al., 2021; Nissen et al., 1995; Pan and He, 2023; Savva et al., 2014; Wan et al., 2019; Wang et al., 2012; Xia et al., 2018; Zhao et al., 2016). In addition, according to their distinct origins, the HVL of the lower crust in this area can be divided into two parts: northwest and southeast. The former is mainly attributed to residual magmatic material of the subduction of the paleo-Pacific Ocean (Cheng et al., 2021; Wan et al., 2017), and the latter is more likely formed by underplating of post-rift magma (Eakin et al., 2014; Lester et al., 2014; Liu et al., 2022; Wan et al., 2019; Wang et al., 2006; Zhao et al., 2010). In particular, the HVL in the Southern Depression of the Southwest Taiwan Basin in southwestern Taiwan has been attributed to mantle serpentinization (Fig. 1) (Chen et al., 2023; Liu et al., 2021; Liu et al., 2023).

At ~18 Ma, the SCS plate subducted eastward under the West Philippine Sea plate, forming the MT (Sibuet et al., 2021). In its northern section, a subduction system consisting of the SCS Basin, the MT, the accretionary wedge (Hengchun Ridge), the forearc basin (North Luzon Trough), and the volcanic arc (North Luzon Arc) is sequentially formed from west to east (Fig. 1) (Ludwig et al., 1979). The continuous subduction caused the Luzon Arc to be close to the rift margin in the northeastern SCS and began to collide at 6–7 Ma to form the Taiwan orogenic belt (Byrne et al., 2011; Huang et al., 2006; Lin et al., 2003; Sibuet and Hsu, 2004; Tan et al., 2022), making this section a typical arc-continent collision setting in the world.

Orogeny in Taiwan has been suggested to go through two stages. The first stage was the initial collision stage, which started approximately 6–7 Ma and was dominated by tectonic underplating formed by the

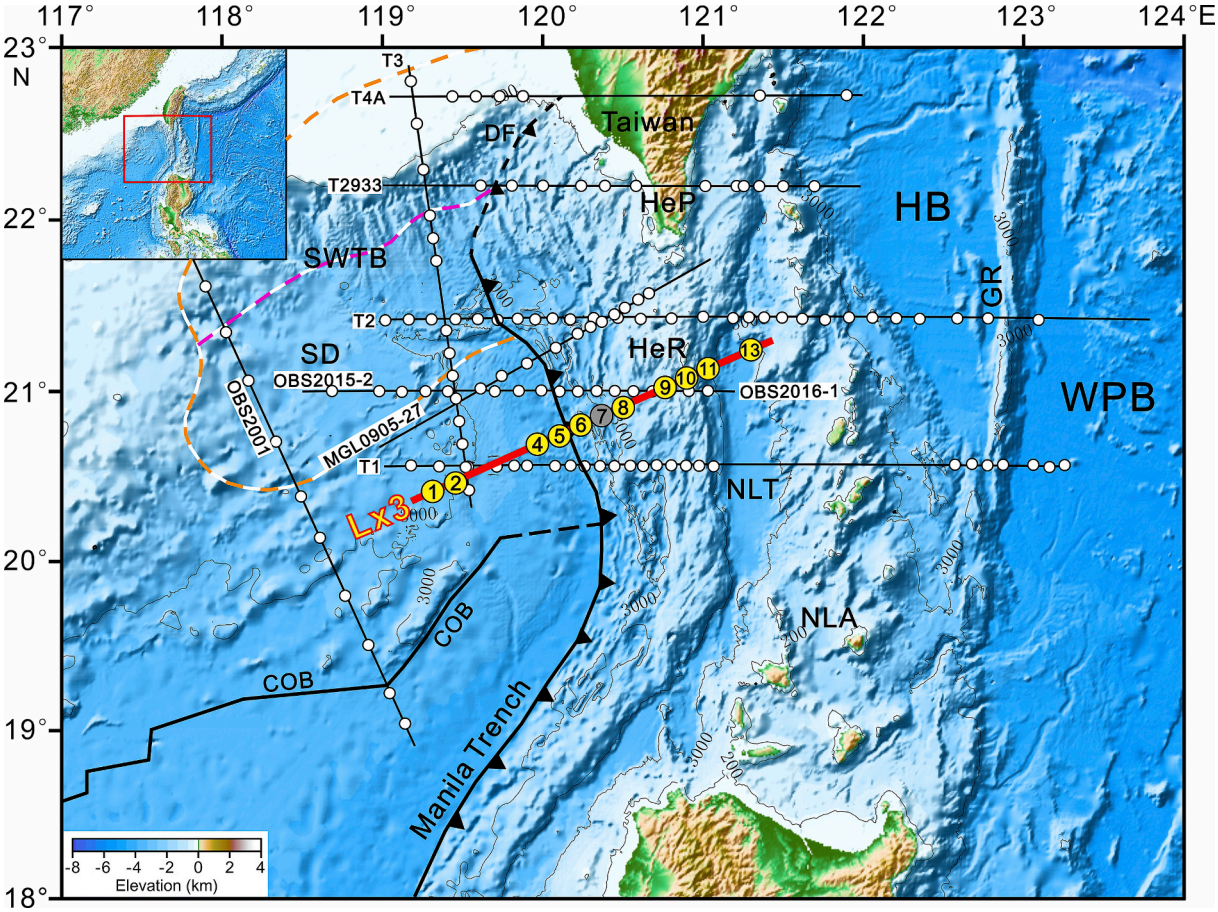

Fig. 1. Bathymetric map of the northeastern South China Sea. The red solid line represents the study profile Lx3, the yellow circles and numbers represent the positions of OBS stations, whereas the grey circle represents the station without usable data. The thin black solid lines and white circles represent the locations of other seismic lines and OBSs in the region, respectively (Eakin et al., 2014; Lester et al., 2013, 2014; Liu et al., 2022; McIntosh et al., 2013; Wang et al., 2006). The black line and triangles represent the Manila Trench (Sibuet et al., 2021). The continent-ocean boundary (COB) is the black solid and dotted line (Liu et al., 2022). The orange and white dashed line represents the Southwest Taiwan Basin (SWTB) boundary, and the purple and white dashed line represents the boundary of the Southern Depression (SD; Chen et al., 2023). HB, Huatung Basin; WPB, West Philippine Basin; GR, Gagua Ridge; HeR, Hengchun Ridge; HeP, Hengchun Peninsula; NLT, North Luzon Trough; NLA, North Luzon Arc; DF, Deformation front. (For interpretation of the references to colour in this figure legend, the reader is referred to the web version of this article.)

subduction of the thinned continental crust (Lester et al., 2013; McIntosh et al., 2013). The second stage was the emerging stage; at 1–2 Ma, the continental crust began to subduct and collide, and the accretionary wedge quickly uplifted and surfaced (Lester et al., 2013; McIntosh et al., 2013; Tan et al., 2022). To Northern Taiwan, the Philippine Sea plate subducted northward along the Ryukyu Trench beneath the Eurasian continental margin (Klingelhoefer et al., 2012). Central Taiwan is experiencing a mature collision between the Philippine Sea plate lithosphere and the Eurasian plate lithosphere. Both horizontal shortening and vertical uplift have reached a maximum, and the topography and thermal properties have reached a steady state, resulting in a mature system of the accretionary wedge model (Beyssac et al., 2007; Chim et al., 2018; Stolar et al., 2007; Willett and Brandon, 2002). In contrast, Southern Taiwan is in the juvenile stage of collision; the southernmost part is experiencing the subduction of the Eurasian plate into the Philippine Sea plate, and the Hengchun Peninsula represents the emergence of an accretionary wedge formed by the subduction of the Eurasian plate along the MT (Simoes et al., 2012; Tsai et al., 2019).

3. Data and method

3.1. Data acquisition and preprocessing

The two-dimensional OBS profile, referred to as Lx3, was recorded in 2016 by *R/V Shiyan 2* of the South China Sea Institute of Oceanology, Chinese Academy of Sciences. The seismic source system used for this profile comprises an array of four airguns with a total volume of 6000 in^3 with a dominant frequency range of 3–8 Hz. 13 OBSs were deployed

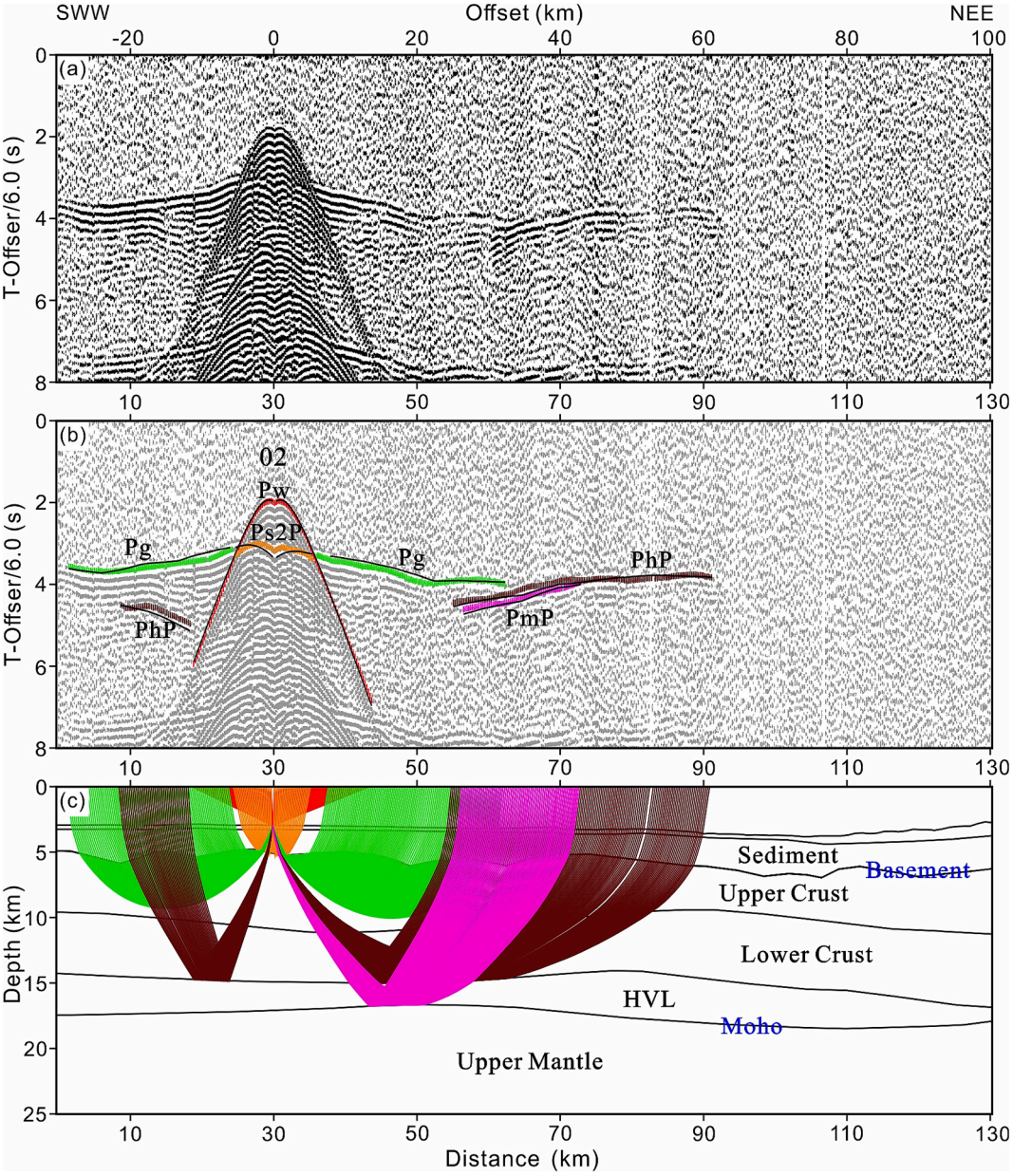

Fig. 2. Ray-tracing and travel times simulation of OBS02. (a) Vertical-component seismic record section of OBS02, and a reduced velocity of 6.0 km/s. (b) Comparison of the calculated travel times (black solid lines) with the observed travel times (colour lines), where Pw is the direct water wave, Ps2P is the reflection phase of the sedimentary layer-2 basement, Pg is the refraction phase within the crust, PhP is the reflection phase of the top interface of the lower crustal high velocity layer, and PmP is the reflection phase of the Moho surface. The colour lines' thickness corresponds to the seismic phases' uncertainties. (c) In the ray-tracing simulation and P-wave velocity model, different colored ray paths correspond to the various colored travel times of the seismic phases in (b). HVL, High velocity layer.

along the profile, and 11 OBSs were recovered. OBS03 and OBS12 were lost, and the recovery rate was 84.6 %. Among them, OBS07 recorded no usable data (Fig. 1). The length of the profile is 256 km, and data acquisition proceeded from northeast to southwest. The number of shots is 1088, the shooting interval is approximately 90 s, and the OBS station spacing is about 15 km. The MCS data along the profile were collected synchronously, with a length of 256 km, 4 receiver channels, and recording length up to 10 s.

The preprocessing of OBS data included raw data transformation, clock drift correction, shot point correction, and OBS location correction. Relocations of the instruments on the seafloor were determined by the direct wave travel times via the Monte Carlo and least-square methods (Du et al., 2018). The raw recorded data were compiled into the Seismic Analysis Code (SAC) format. Then, the effective signal segments in the SAC data are selected and converted into the Society of Exploration Geophysicists (SEGY) format. The information preserved for each trace includes the shot number, shot time, latitude and longitude coordinates, and water depth of the shot point in the navigation file and the timer file (Qiu et al., 2011; Zhang et al., 2012). Finally, the seismic processing software package Seismic Unix (SU) (Stockwell and Cohen, 2002) is used to filter and gain the SEGY files (Wang et al., 2016; Zhang et al., 2018; Zhang et al., 2019) to compile a seismic record profile with clear seismic phases such as PsP, Pg, and PmP (Figs. 2, 3 and 4).

The Lx3 profile's MCS data are processed via format transformation, eliminating invalid shot points, cutting and splicing, etc., and the MCS profile is drawn using SU software for filtering, automatic gain control, and other processes (Fig. 5).

3.2. Travel-time picking and initial model construction

A total of 4789 arrivals were manually picked up on Profile Lx3, including 1016 direct water wave arrivals (Pw, for relocation of OBSs), 1928 refraction arrivals (Ps, Pg and Pn, representing refracted from the sediments, crust and upper mantle, respectively), and 1845 reflection arrivals (PsP, PaP, PhP and PmP, representing reflected from the sediment interfaces, the bottom of the low-velocity anomaly, upper interface

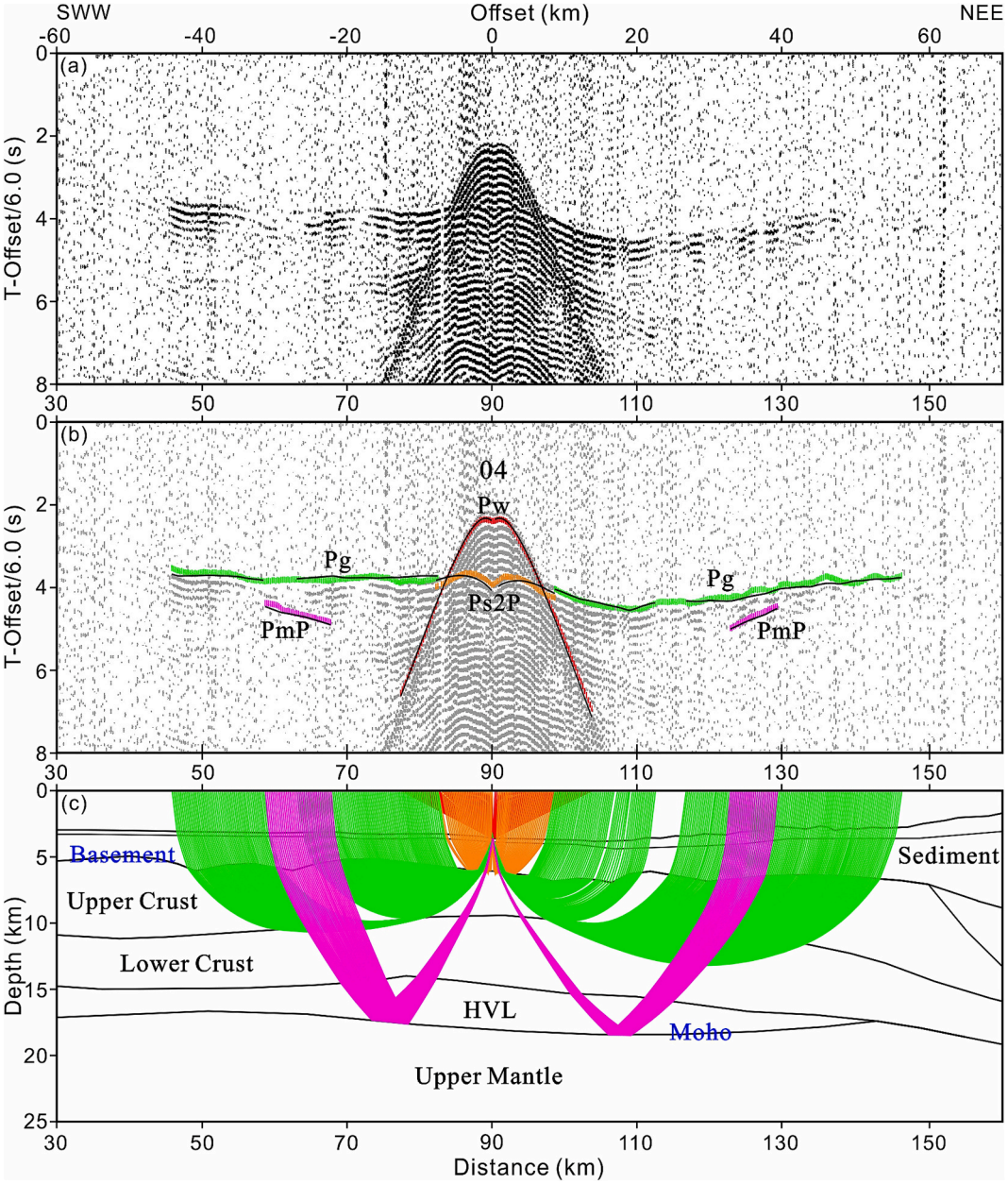

Fig. 3. Ray-tracing and travel times simulation of OBS04. See the caption of Fig. 2 for details.

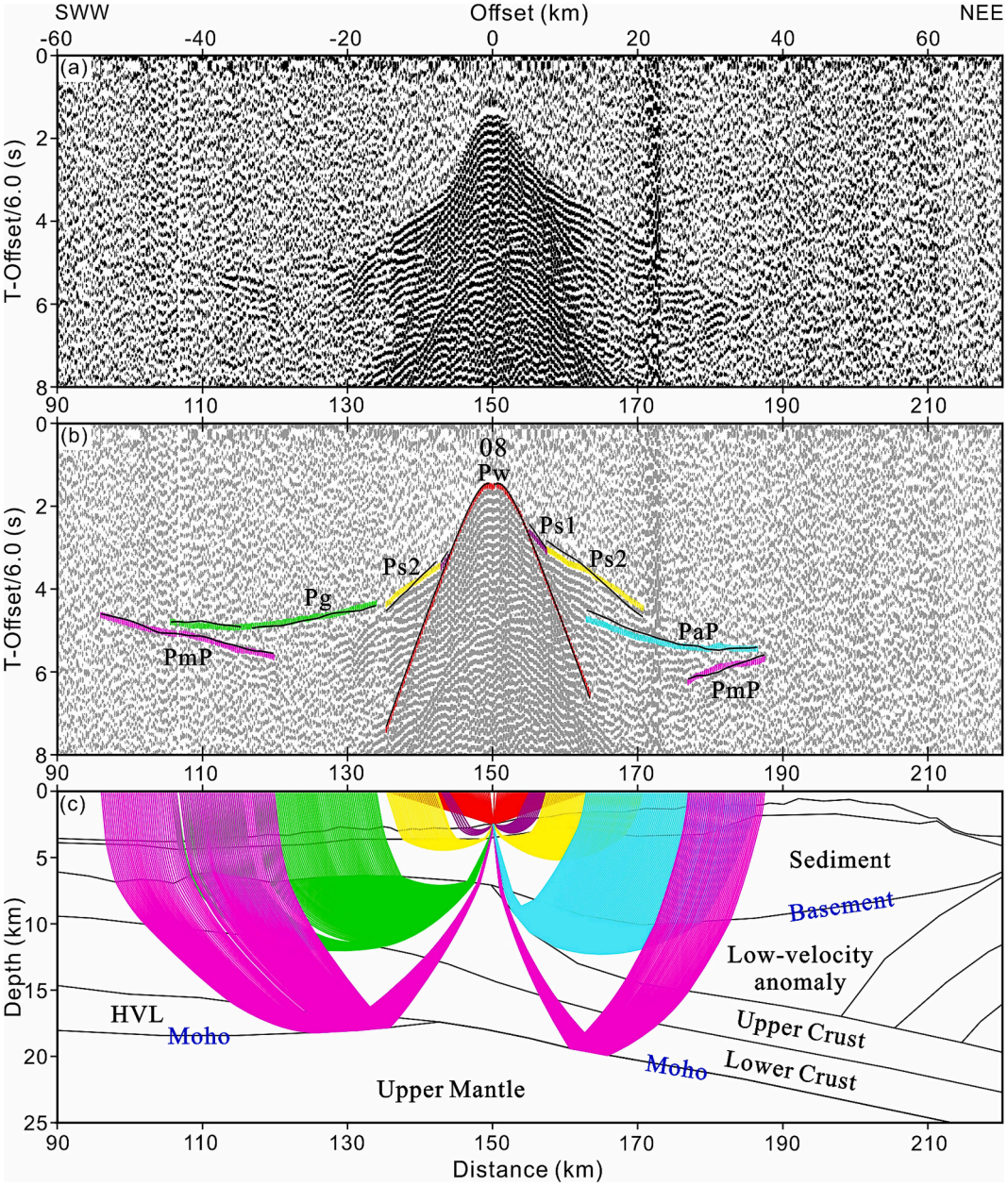

Fig. 4. Ray-tracing and travel times simulation of OBS08. See the caption of Fig. 2 for details. Ps is the refracted seismic phase in the sedimentary layer, and PaP is the reflection phase of the bottom interface of a low-velocity anomaly.

of the HVL, and bottom of the Moho, respectively) (Table 1). According to the empirical parameterization of Zelt and Forsyth (1994), the uncertainty range of picking is 50–100 ms (Figs. 2, 3 and 4).

The OBS02 station (Fig. 2) observed the reflection phase of sedimentary layer-2, and the Pg phase is visible, which is observed in the range of −5 ~ −30 km on the west side and 6–34 km on the east side. The PhP phase can be traced to −12 ~ −22 km on the west and 25–62 km on the east. The PmP phase can be traced to 27–43 km. The OBS04 station (Fig. 3) also identified the reflection phase of sedimentary layer 2, and the Pg phase has a wide range, which can be traced to −7 ~ −45 and 5–56 km. The PmP phase is difficult to identify and is only observed in the range of −22 ~ −32 km on the west and 33–39 km on the east. At the OBS08 station (Fig. 4), sedimentary layers 1 and 2 refraction phases can be identified. Compared with OBS02 and 04 stations, sedimentary layer-1 was significantly thicker. The Pg phase only occurs within the range of −16 ~ −45 km of the west half branch, indicating that the terrain on the east side has changed significantly. The PaP phase can be traced to 12–39 km, and the PmP phase is identified on both the west and east sides.

We try our best to trace the PmP arrivals for all stations. However, the PmP arrivals are not identified near offsets because they are affected by direct water wave phases with intense energy. Moreover, the PmP arrivals are also affected by the first arrivals (Ps, Pg) traveling in the sediment and crust, respectively, when the PmP acts as second arrivals. Meanwhile, our data shows intense energy associated with free-surface multiples (Figs. 2, 3 and 4). We only picked up the fastest one as the first wave phase for multiple parallel phases (Figs. 2a, 3a and 4a) formed due to the decay of the energy. In addition, we find multiple waves associated with other interfaces in Fig. 2a (at positions around 8 s). We use the seafloor bathymetry of the OBS station to calculate multiple waves associated with the seafloor or at other interfaces.

The *RayInvr* software (Zelt and Smith, 1992) is used for forward modeling, and the theoretical travel times are consistent with the observed travel times via the trial-and-error method. The length of the

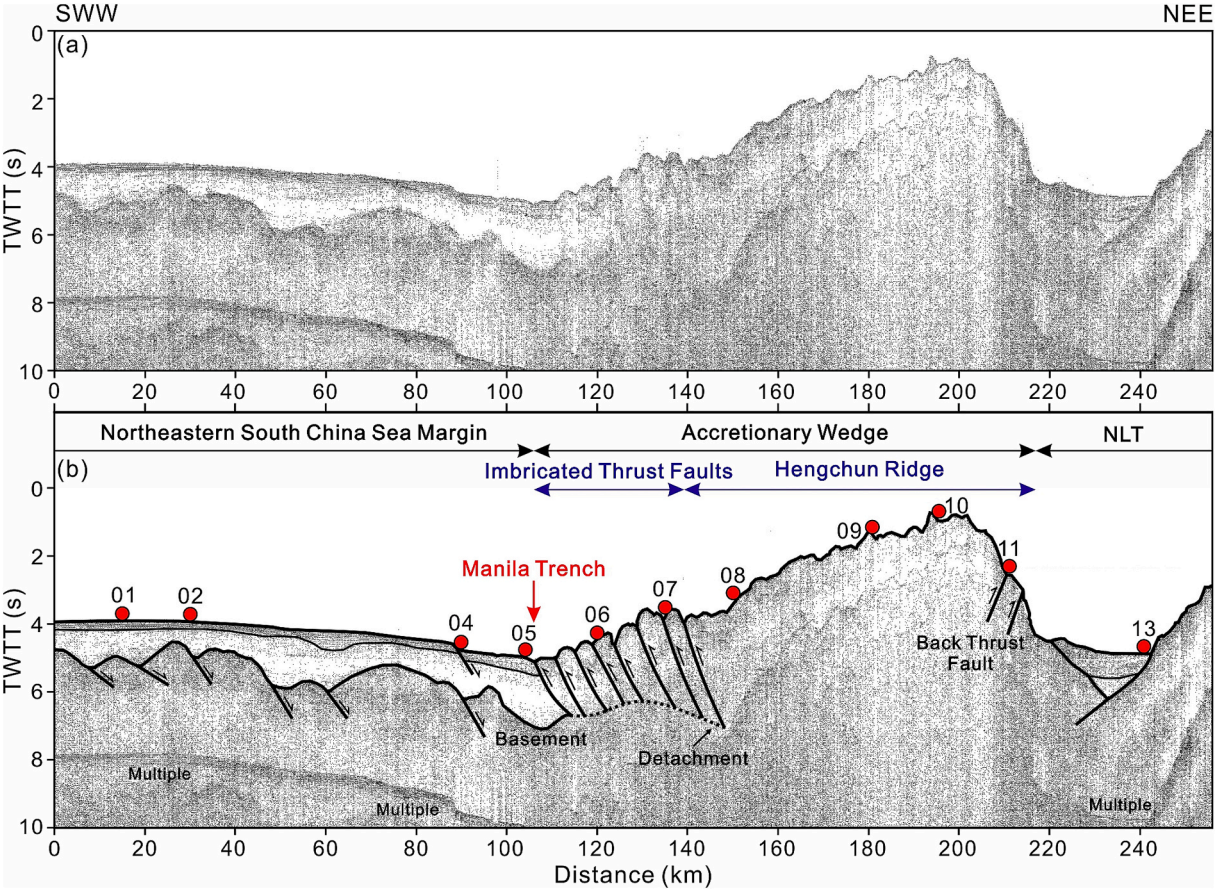

Fig. 5. (a) Original multi-channel reflection seismic profile acquired by *R/V Shiyan 2*. (b) Interpretation of multi-channel reflection seismic profile. The red circles represent OBS stations. NLT, North Luzon Trough. (For interpretation of the references to colour in this figure legend, the reader is referred to the web version of this article.)

Table 1
RMS misfit, χ^2 values, and picking errors for each seismic phase from forward modeling of Profile Lx3.

Phases	Travel-times	RMS (ms)	χ^2	Picking errors (ms)
Pw	1016	79	1.112	50
Ps	284	124	2.761	75
PsP	465	104	1.916	75
PaP	128	113	2.293	100
Pg	1542	82	1.198	50
PhP	382	96	1.653	75
PmP	870	83	1.224	75
Pn	102	124	2.774	100
total	4789	90	1.428	

model is 256 km, and it is divided into six layers, including seawater, sediment layer 1, sediment layer 2, upper crust, lower crust and upper mantle, with velocities of 1.5 km/s, 2.0–2.5 km/s, 3.0–3.5 km/s, 5.0–6.4 km/s, 6.4–7.0 km/s and 8.0–8.2 km/s, respectively. In the process of forward modeling, the accuracy of the initial forward model greatly influences the final model, and it is also the basis of forward ray-tracing. The accuracy of the structure of the shallow sedimentary layer directly affects the accuracy and efficiency of *RayInvr* forward trial and error simulation. For maximum accuracy, the seafloor and sedimentary interfaces of the model are determined mainly by the MCS data.

The *Tomo2d* is an inversion software (Korenaga et al., 2000) that involves joint refraction and reflection travel times. It uses the least squares orthogonal decomposition method to solve linear equations and invert the information of the underground velocity structure. Much less prior information was used, and the results were more objective. In the inversion process, the velocity in the crust is continuous, and the reflection interface is a floating interface, so the velocity grid and reflection interface are independent of each other. We include the basement geometry and sediment velocities from the initial forward model for the initial inversion model. We set the velocity to be 8.2 km/s at a depth of 30 km. The corresponding parameters are selected according to the length of the seismic profile, the number of OBS stations, and the seismic phases.

4. Velocity structure

4.1. Forward velocity modeling by RayInvr

The final forward velocity structure, ray coverage density, and comparison between the calculated and observed arrivals obtained using *RayInvr* (Zelt and Smith, 1992) of Profile Lx3 are shown in Fig. 6. The model is divided into eight layers: seawater (1.5 km/s), sediment layer 1 (2.0–2.5 km/s), sediment layer 2 (3.0–3.5 km/s), low-velocity anomaly (4.8–5.5 km/s), upper crust (5.0–6.4 km/s), lower crust (6.4–6.7 km/s), HVL (7.1–7.5 km/s) and upper mantle (8.0–8.2 km/s). The total RMS of the model fit with the data is 90 ms, and the final normalized χ^2 is 1.428 (Table 1), indicating that the calculated travel times fit well with the observed travel times and that the model is close to the reality model. It can be seen from the ray coverage density (Fig. 6b) that the number of ray coverages in most regions is more than ten times. The central area with dense stations and a high degree of ray crossover is more than 30 times or even more than 100 times greater. Except for the two ends of the model and the accretionary wedge, the other parts of the Moho plane are relatively dense, which effectively

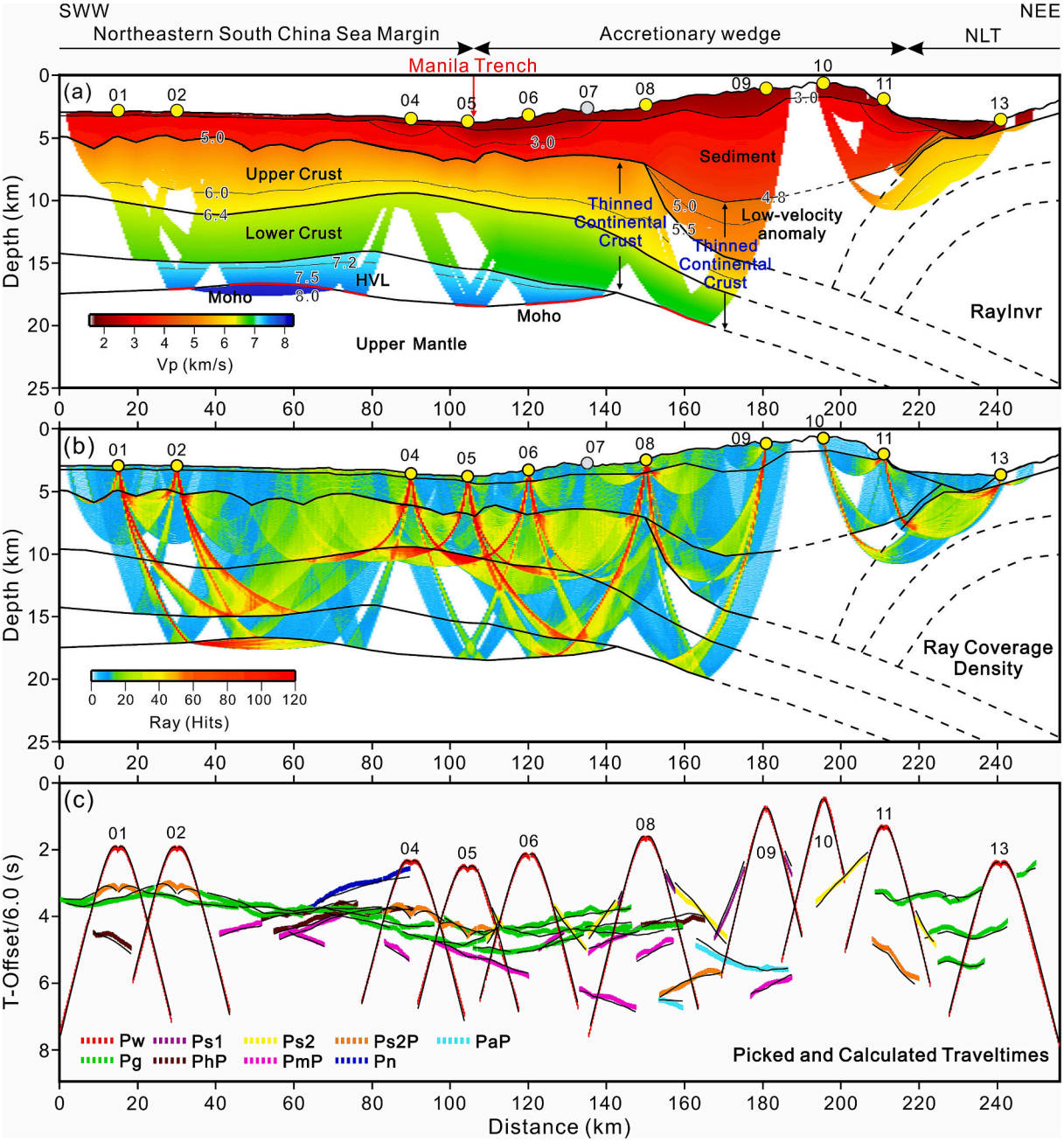

Fig. 6. The forward P-wave velocity structure along profile Lx3. (a) Preferred final forward velocity model using *RayInvr* software (Zelt and Smith, 1992). The thick red segments indicate where PmP arrivals constrain the Moho interface and the dotted lines represent the uncertain interface without ray coverage. The yellow circles represent OBS stations. (b) Ray coverage density on a 0.25 km × 0.25 km grid. (c) Picked (colored) and calculated (black) traveltimes of seismic phases for all OBS receivers in the model. NLT, North Luzon Trough; HVL, High velocity layer. (For interpretation of the references to colour in this figure legend, the reader is referred to the web version of this article.)

restricts the velocity structure.

4.2. Inverse velocity modeling by Tomo2d

An approach of combining different modeling techniques is the most promising way to image the deeper layers of the Earth since deep crustal structure stays out of reach of direct sampling efforts. To confirm the validity of the *RayInvr* model, an inversion simulation was performed using *Tomo2d* software (Korenaga et al., 2000), and the inversion velocity structure was obtained (Fig. 7). Although *Tomo2d* requires less prior information than *RayInvr*, and does not need to adjust the position and velocity of nodes, it has many inversion parameters. We tested several parameters to establish the initial model. The horizontal correlation length is 1–1.5 km, and the vertical correlation length is 1–2 km. The correlation length of the Moho reflector is 9 km. After three iterations, the RMS misfit of the final velocity model converges to 75.5 ms, and the final χ^2 value is 1.014.

The geometric shapes of the forward and inversed Moho surfaces are the same within the 0–140 km distance range of the model (Figs. 6 and 7), and the depth is between 17–19 km. However, the Moho surface differs significantly in the range of 140–256 km due to the poor propagation of rays in the accretionary wedge and the sparse ray coverage at the model's margin. In this case, the Moho surface of the forward model in this region is depicted from the results of adjacent seismic lines. In

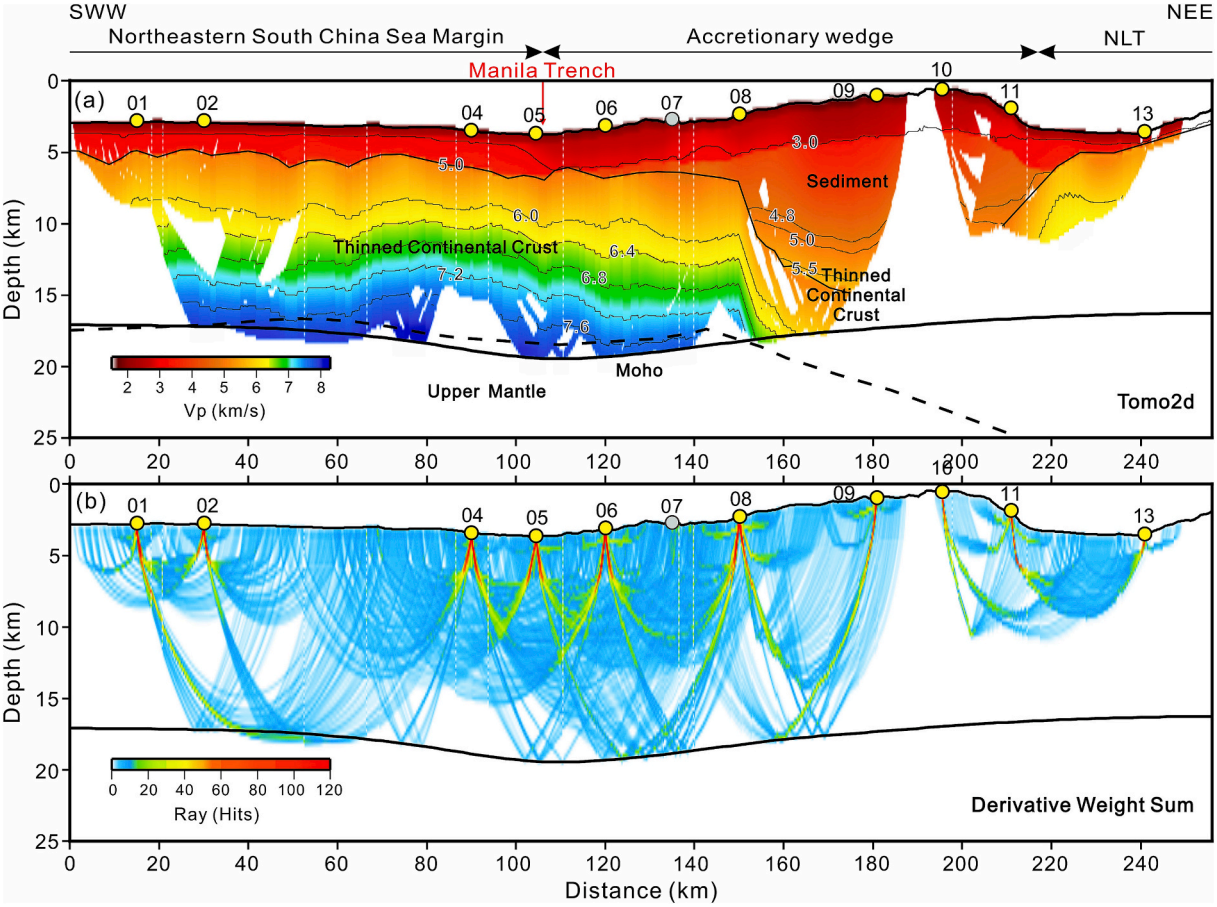

Fig. 7. Final inverted velocity model of Lx3 using *Tomo2d* software (Korenaga et al., 2000). (a) Inversion velocity model using the *Tomo2d* software with a floating Moho interface (solid black line). The dashed black line indicates the Moho interface from the *RayInvr* model (Fig. 6). (b) Derivative weight sum (DWS) of profile Lx3 showing ray coverage throughout the model.

addition, except for the region with poor ray coverage, the crust thickness of the forward and inversion models is approximately 12–15 km, characteristic of thinned continental crust. The model results obtained by *RayInvr* and *Tomo2d* are roughly consistent, indicating that the preferred final velocity model (Fig. 6) is reliable.

5. Interpretations and analysis

5.1. Analysis of the P-wave velocity structure along profile Lx3

According to the seafloor topography, MCS profile and P-wave velocity structure (Figs. 1, 5, 6 and 7), profile Lx3 is divided into three regions from west to east: 0–107 km is the northeastern SCS margin, 107–217 km is the accretionary wedge, and 217–256 km is the North Luzon Trough.

The shallow sediment strata in the range of 0–107 km was not strongly deformed and divided into two sediment layers with P-wave velocities of 2.0–3.0 km and 3.0–3.5 km/s, respectively. The crustal thickness is approximately 12–15 km, which belongs to the thinned continental crust of the SCS. We used *MATLAB* programs to extract the velocity values below the basement under each station from the final *RayInvr* and *Tomo2d* velocity structures (Fig. 8). Among them, the results of one-dimensional velocity-depth profiles beneath the OBS01 to OBS05 stations also reveal that this area consists of thinned continental crust (Fig. 8). The sediment layer's low seismic velocity (2.7 km/s) below the OBS04 station and the presence of normal faults, as observed in the MCS profile (Fig. 5), may be related to plate bending. The MT is located at 107 km, and there is a HVL of the lower crust at 0–142 km, with a velocity of 7.1–7.5 km/s. Previous studies of Vp/Vs indicate that the HVL in this area is a product of magmatic underplating (Wen et al., 2021a, 2021b; Zhao et al., 2010).

The 107–217 km distance range corresponds to the accretionary wedge. The sediment velocity decreases to 2.3–2.5 km/s at the distance range of 107–139 km, which corresponds well to the imbricated thrust faults in the MCS profile (Fig. 5), and the sediment velocity decreases because water enters the fault zone. The crustal thickness is ~13 km. The distance range of 139–217 km is the Hengchun Ridge. Due to plate subduction, most of the material is scraped off and deposited on the overlying plate, resulting in a ~ 78 km thick accretionary wedge. This sediment accumulation leads to strong attenuation of seismic signals, and the deep structure of the ridge cannot be well constrained. However, from the one-dimensional velocity-depth profiles below the OBS06 to OBS09 stations, it can be seen that the subducted crust belongs to the thinned continental crust of the SCS (Fig. 8). The results obtained by OBS08 and 09 stations ray-tracing reveal that there is a low-velocity anomaly (4.8–5.5 km/s) in the lower part of the accretionary wedge compared to the subduction plate on the west side at the model distance range of 150–215 km. The nature and genesis of the low-velocity anomaly will be discussed in section 6.1 below. The velocity of the sediment layer below the OBS11 is small, approximately 2.5 km/s, corresponding to the back thrust faults of the Hengchun Ridge.

The distance range of 217–256 km is the North Luzon Trough. OBS13 is located east of the North Luzon Trough, and together with OBS11, it yields the smaller velocity value (1.7–2.3 km/s) of the sediment layer in the trough.

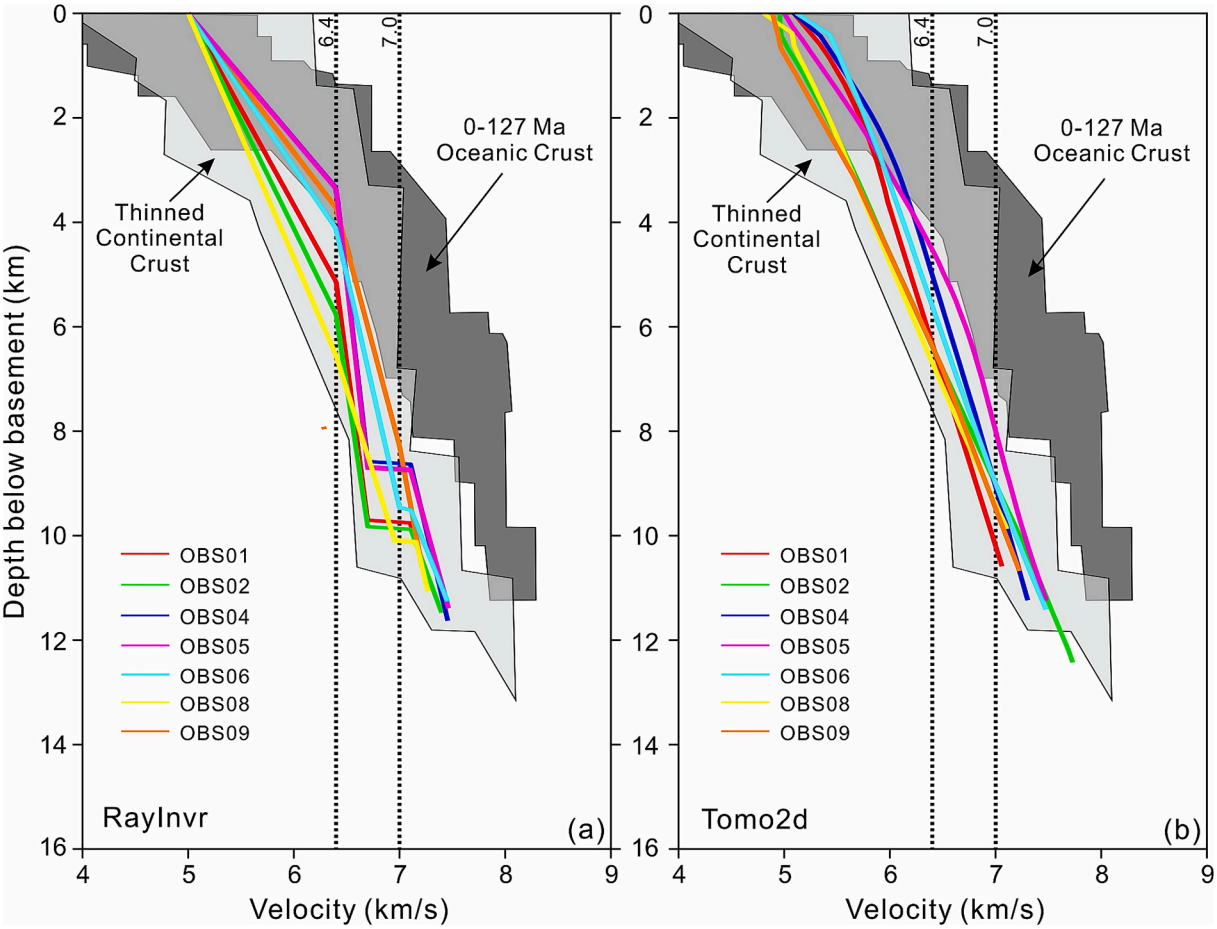

Fig. 8. 1D velocity model along Profile Lx3. (a) 1D profiles extracted from the final *RayInvr* velocity model; (b) 1D profiles extracted from the final *Tomo2d* velocity model. The dark grey area indicates the range of typical velocities for the oceanic crust (White et al., 1992). The light grey area indicates the area of thinned continental crust (Nissen et al., 1995; Qiu et al., 2001; Wang et al., 2006; Yan et al., 2001).

5.2. Multi-channel seismic profile interpretations

MCS profile Lx3 clearly shows the trend of plate subduction, the topography of the accretionary wedge and the forearc basin (Fig. 5). In the northeastern SCS margin, the plate has not yet entered the accretionary wedge and has not been affected by subduction, and the stratigraphic continuity is good. We divided two layers of sediment; the thickness of sediment layer 1 is approximately 0.3 s, and the thickness of sediment layer 2 is approximately 1 s. A small number of normal faults are observed in this region, which may be related to the subduction and bending of the lithosphere. The basement is highly undulating and consists of many inclined fault blocks, possibly associated with extensional stretching during the rift period and magmatic intrusion during the post-rift period (Chiu et al., 2021). The front of the Hengchun Ridge features imbricated thrust faults and rugged topography, which gradually uplifted from west to east. The bottom of the thrust fault is a detachment fault. The Hengchun Ridge is the uplift deformation section; the accretionary wedge strongly uplifted, and the internal deformation of the strata was significantly deformed, which led to the poor propagation of seismic signals in the area and the inability to identify the internal structure. The back thrust faults are identified in the eastern part of the Hengchun Ridge. They may have been formed by the continuous thrust extrusion of the imbricated thrust faults to the North Luzon Trough or the compressional structure caused by the subduction of seamounts (Li et al., 2013; Wang et al., 2019). Two layers of sediment are also identified inside the North Luzon Arc, with an approximate thickness of ~0.7 s. Due to continuous subduction and the thickening and uplifting of the accretionary wedge, the North Luzon Arc has been persistently deformed (Eakin et al., 2014).

5.3. Gravity modeling and density variation features

Gravity data are more sensitive to lateral variations in subsurface densities, such as at subduction zones (Kashubin et al., 2017). Observed gravity data are extracted from the global gravity dataset with a 1 min × 1 min resolution (Sandwell et al., 2013). The density values of the seawater and homogenous mantle are assumed to 1.03 g/cm^3 and 3.28 g/cm^3, respectively. The density of the sediment layer is calculated according to Hamilton's (1978) empirical law, whereas the crustal density is obtained from Christensen and Mooney's (1995) empirical law. *MASK* simulation software (Yao et al., 2003) calculates the model's free-air gravity anomaly. More importantly, we extended the model by 50 km on both sides to eliminate the influence of edge effects (Dean et al., 2000).

The final gravity model shows that the calculated gravity anomaly fits well with the observed gravity anomaly (Fig. 9), and the RMS misfit is 3.62 mGal. The accretionary wedge is being compacted to some extent due to compression, resulting in denser sediment (2.10–2.55 g/cm^3) than the subduction front (2.10–2.40 g/cm^3) and the North Luzon Trough (1.90 g/cm^3). The density of the low-velocity anomaly beneath the accretionary wedge is 2.65 g/cm^3. At approximately 160 km, the crustal density increases from 2.68 to 2.85 g/cm^3 to 2.72–2.87 g/cm^3, likely caused by higher pressures. The lowest gravity anomaly is distributed along the North Luzon Trough, reflecting the uplift of the accretionary wedge.

The results of the gravity simulation inversion based on the velocity

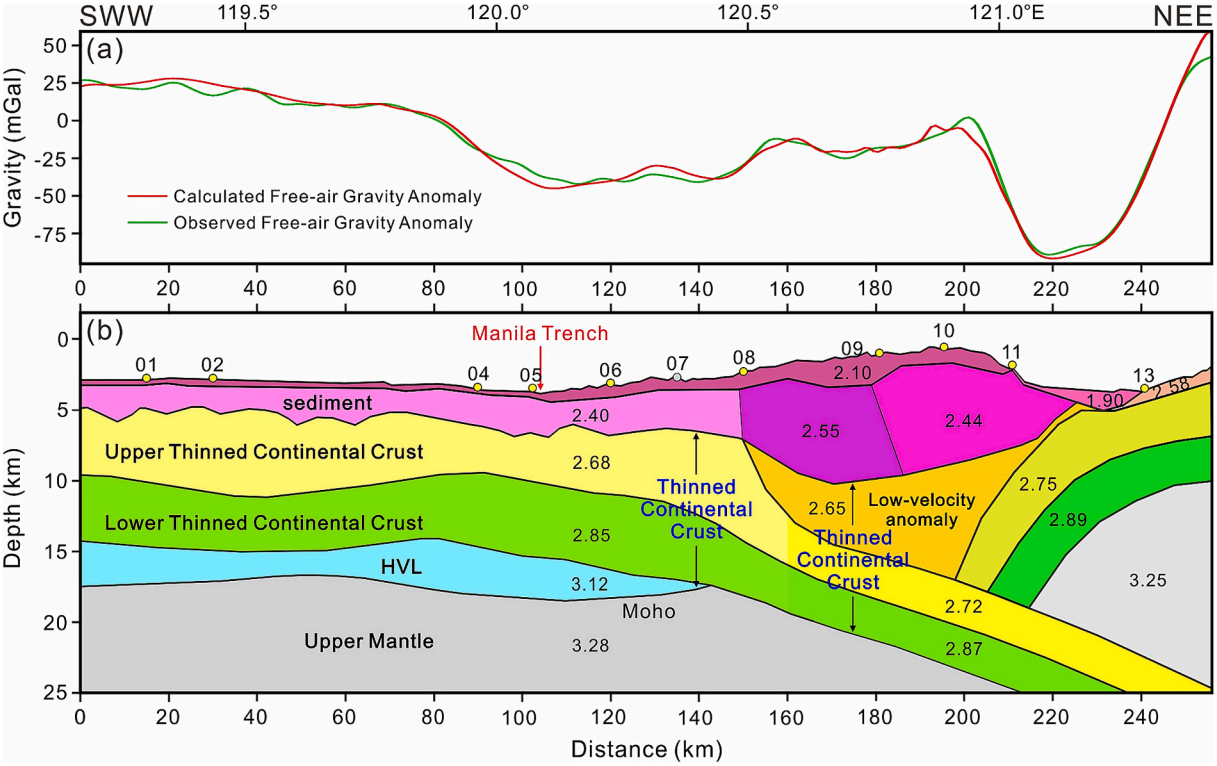

Fig. 9. Free-air gravity modeling and magnetic anomalies along Profile Lx3. (a) Observed (green) and calculated (red) free-air gravity anomalies. (b) Best-fit 2D gravity model of Profile Lx3 with densities in g/cm^3. (For interpretation of the references to colour in this figure legend, the reader is referred to the web version of this article.)

model interface are well-fitted to the globally observed gravity anomalies (Fig. 9), which additionally indicates the validity and reliability of our models (Figs. 6a and 7a).

6. Discussion

6.1. Velocity anomaly at the base of the accretionary wedge

A velocity anomaly was observed at the base of the accretionary wedge along previous seismic lines in the northeast SCS, which has been hypothesized to be related to the structurally underplating of thinned continental crust to the base of the accretionary wedge (Eakin et al., 2014; Lester et al., 2013; McIntosh et al., 2013). However, according to the high density found at the bottom of the accretion wedge through gravity modeling, Doo et al. (2015) & Doo et al., 2016) speculated that it was the result of dehydration of the subducting Eurasian Plate, leading to the serpentinized fore-arc mantle, which was then exhumed along the subduction channel due to its positive buoyancy and weak coupling at the subduction interface.

A velocity anomaly (4.8–5.5 km/s) is also observed at the base of the accretionary wedge within 150–215 km along the Lx3 profile (Fig. 6). Our velocity model (Fig. 6) and gravity model (Fig. 9b) indicate that this structural anomaly with a velocity of 4.8–5.5 km/s and density of 2.65 g/cm^3 are similar to the top of the upper crust of the subducted thinned continental crust (5.0–5.5 km/s and 2.68 g/cm^3). Therefore, it is speculated that during the early rifting-breakup period, rift-related faults and detachments contributed to the thinning of the continental crust, which included many fault blocks in the upper crust. During the subduction process, these fault blocks may have scraped off and accreted to the bottom of the accretionary wedge in the eastern part of the trench. Then, the subduction plate underwent metamorphic dehydration when temperature and pressure increased during subduction. So, we further hypothesize that water released from the subducting plate upward migrates to the overriding lithosphere, resulting in a low-velocity anomaly. The “low-velocity anomaly” here refers to the lower velocity relative to the subducting plate on the west side.

To characterize of the velocity anomaly at the bottom of the accretionary wedge associated with various subduction processes with different crustal properties, P-wave velocity structure imaging of seven OBS profiles were collected in the northeast SCS (Fig. 10a). We refer to the Manila transcurrent fault (MTF) proposed by the previous study (Sibuet et al., 2021) as the eastern boundary of the accretionary wedge (Fig. 10). In the southernmost T1 profile, the subduction of the oceanic crust has just completed. The subduction of the thinned continental crust is about to start (Eakin et al., 2014), leading to an oceanic subduction setting. No velocity anomaly is detected at the bottom of the accretionary wedge (Fig. 10h). In contrast, in the south, the MGL0905_27, Lx3, T2, and OBS20152-OBS2016_1 profiles represent the subduction of the thinned continental crust, and low-velocity anomaly is observed at the base of the accretionary wedge (Fig. 10 b, c, f and g). When the thinned continental crust subducted, the upper crust was scraped off and accreted at the base of the accretionary wedge. With the subduction proceeding, with the increase of temperature and pressure, the subducting plate undergoes a metamorphic dehydration reaction, and fluids move upward, leading to the observed low-velocity anomaly. The T4A and T2933 profiles in the north cross the southern tip of the Taiwan orogenic belt (McIntosh et al., 2013). The collision of the continental crust on the South China continental margin strongly uplifted the accretionary wedge. The upper crust material of the scraped subduction plate was uplifted with the accretionary wedge by upward thrusting and compaction. Because it has been avoiding the subsequent dehydration of the subduction plate, and the compaction-induced velocity is greater than that of the subduction plate on the west side, showing a high-velocity anomaly (Fig. 10d and e).

In summary, in the northeast of the SCS, oceanic crustal subduction has limitedly influenced the thickness and width of the accretionary

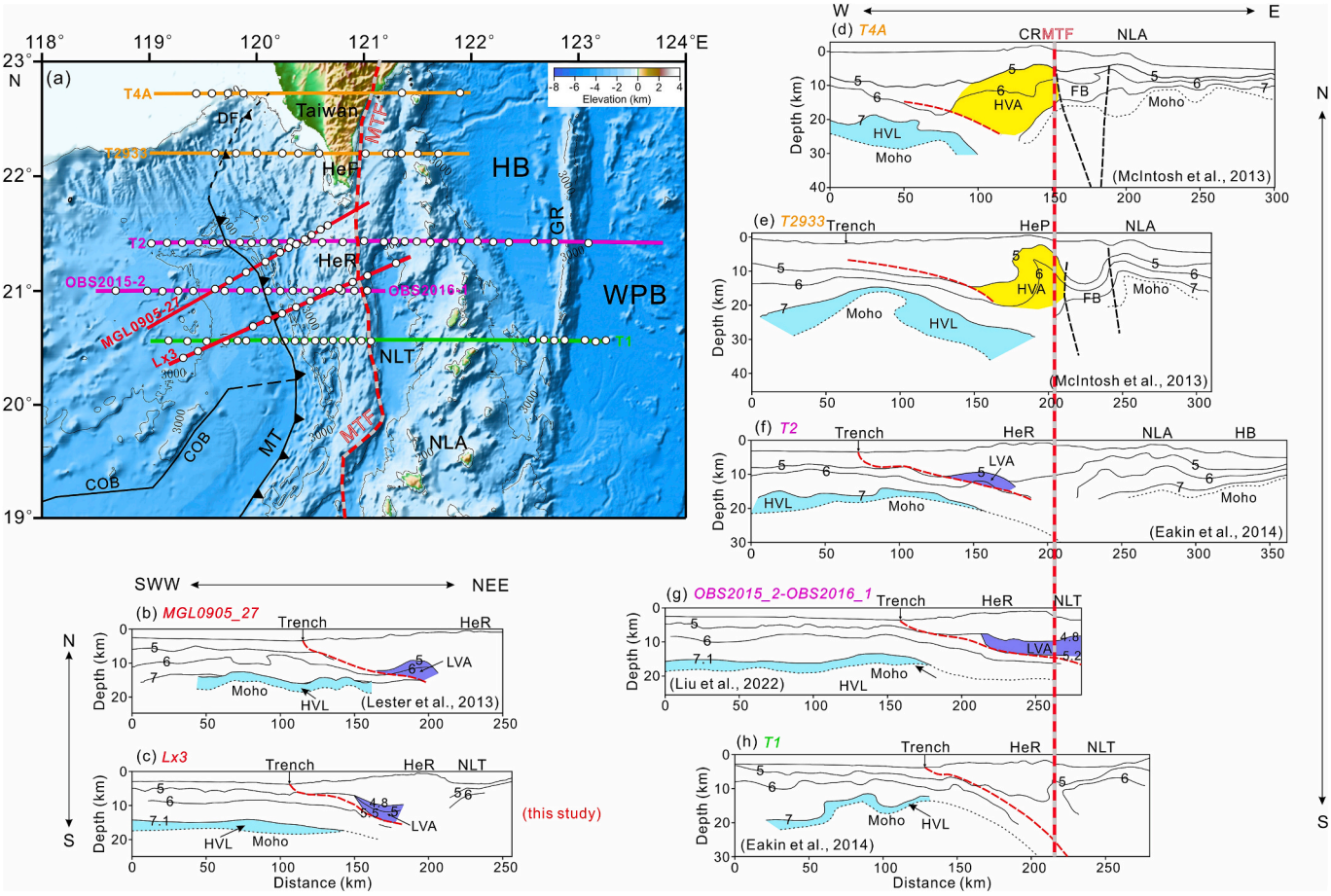

Fig. 10. Comparison between P-wave velocity structures MGL0905_27 (Lester et al., 2013), Lx3, T2 and T1 (Eakin et al., 2014), OBS2015_2-OBS2016–1 (Liu et al., 2022), T4A and T2933 (McIntosh et al., 2013). North of 19°N, the accretionary wedge is located between the Manila Trench (MT) and the Manila transcurrent fault (MTF, red and grey dashed line, Sibuet et al., 2021). WPB, West Philippine Basin; HeR, Hengchun Ridge; HeR, Hengchun Peninsula; NLT, North Luzon Trough; NLA, North Luzon Arc; HB, Huatung Basin; COB, Continent-Ocean boundary; DF, Deformation front; CR, Central Ridge; FB, Forearc Backstop; HVL, High velocity layer; LVA, Low-velocity anomaly; HVA, High-velocity anomaly. (For interpretation of the references to colour in this figure legend, the reader is referred to the web version of this article.)

wedge, and no apparent velocity anomaly is formed at the bottom of the wedge. In contrast, during the transition from thinned continental crust subduction to arc-continental collision, the anomaly in the bottom of the accretionary wedge changes from low-velocity to high-velocity, more likely due to the transition from hydration to compaction in response to the tectonic shift. (Fig. 10).

6.2. *Tectonic evolution model for the transition from subduction to collision*

Combining the results of Lx3 with previous seismic and other geophysical surveys, a tectonic evolution model of the transition from subduction to arc-continental collision in the northeast SCS is proposed (Fig. 11). The evolution model can be divided into four regimes according to the differences in the properties of subducting plates.

In the first regime, which probably occurs south of 20.2°N, the oceanic crust is subducted under the Luzon arc of the Philippine Sea Plate. Because there is less sediment, thanks to being far from the continental margin of South China, the oceanic crust is thin, and the basement is relatively flat, forming a small accretionary wedge without observable velocity anomaly and developing a forearc basin (North Luzon Trough) (Fig. 11a).

In the second regime, between 20.2°N and 21.5°N, the thinned continental crust is initially subducted, accompanied by the accretionary wedge gradually widening and the forearc basin narrowing progressively. At this regime, due to the subduction of the thinned continental crust, the fault blocks of the upper crust were partially scraped off and accreted to the bottom of the accretionary wedge, causing the accretionary wedge to thicken and the formation of a low-velocity anomaly due to the hydration effect of plate dehydration (Fig. 11b).

In the third regime, the initial collision occurs at 21.5°N ~ 22.7°N. The continental crust begins to subduct. Meanwhile, the North Luzon Trough completely closes, and the accretionary wedge is heavily uplifted, widened, and finally emerges above the water level. The low-velocity anomaly underplating at the bottom of the accretionary wedge formed in the second regime suffers subsequent compression and compaction and then turns into a high-velocity anomaly (Fig. 11c).

In the final regime, mature collision happens to the north of 22.7°N, the passive continental margin of the Eurasian plate continued to collide with the Luzon Arc, forming a typical active arc-continental collision orogenic belt that is taking place at Taiwan at present (Fig. 11d). The high-velocity anomaly at the base of the accretionary wedge formed in the early regime may be exhumed to the surface (Byrne et al., 2024). To the east, the Coastal Range is mainly composed of Miocence Luzon Arc volcanic rocks, representing the northernmost extension of the Luzon Arc. Further west, separated by the Longitudinal Valley, the units exposed in the Central Range are defined by the slate belt (Hsuehshan Range and Backbone Slates) and polymetamorphic rocks (Tananao Complex) (Molli and Malavieille, 2010). In the foreland, the Western

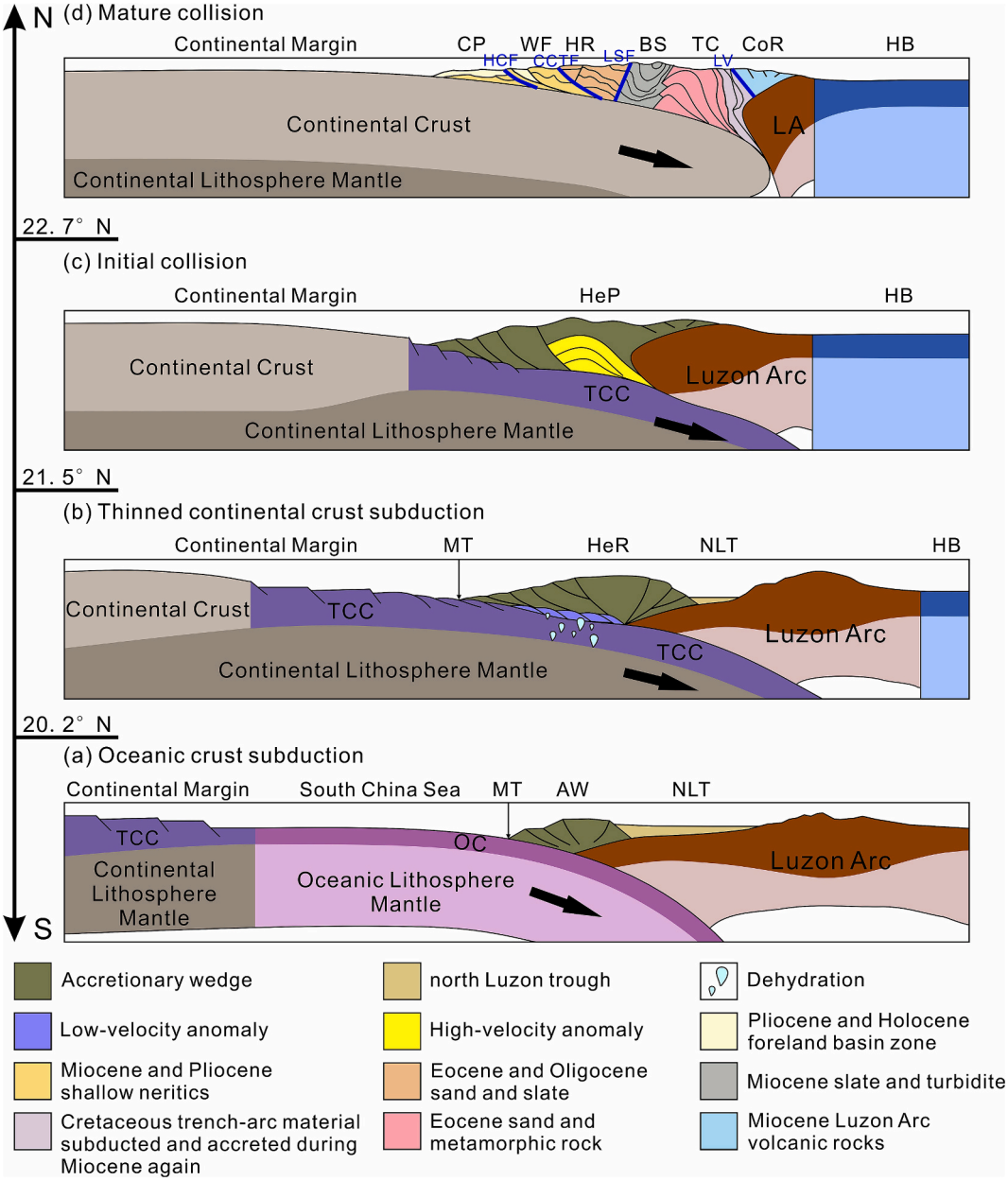

Fig. 11. Tectonic evolution model from subduction in the SCS to arc-continental collision in Taiwan. OC, Oceanic crust; TCC, Thinned continental crust; MT, Manila Trench; AW, Accretionary wedge; NLT, North Luzon Trough; HeR, Hengchun Ridge; HB, Huatung Basin; HeP, Hengchun Peninsula; LA, Luzon Arc; CP, Coastal Plain; WF, Western Foothills; HR, Hsuehshan Range; BS, Backbone Slates; TC, Tananao Complex; CoR, Coastal Range; HCF, Hsingchuang Fault; CCTF, Chuchih Thrust Fault; LSF, Lishan Fault; LV, Longitudinal Valley.

Foothills correspond to a fold-and-thrust belt affecting the Miocene-Pliocene shallow neritics of the Chinese margin and the Pliocene-Holocene deposits of the foreland basin (Xu et al., 2022).

7. Conclusion

The crustal structure obtained from seismic refraction/wide-angle reflection and MCS data on line Lx3 in the northeast SCS, combined with the results obtained by previous studies, provides new insight into the subduction of different natures of the crust in response to subduction to collision processes. The main conclusions are as follows:

1) The nature of the northeastern margin of the SCS is a 12–15 km thick thinned continental crust with a 2–4 km thick HVL of the lower crust formed by magmatic underplating.
2) At the bottom of the accretionary wedge, a low-velocity anomaly is observed with a velocity of 4.8–5.5 km/s, likely formed by the subducted upper crust being partly scraped off and accreted in the wedge, thanks to subsequent hydration, resulting in a low-velocity nature.
3) A tectonic evolution model of the transition from oceanic subduction to arc-continental collision is proposed. In this model, the velocity anomaly at the bottom of the accretionary wedge undergoes a process from ordinary to low-velocity anomaly and then to high-velocity anomaly due to the transition from hydration to compaction.

CRediT authorship contribution statement

Xingyue Wang: Writing – review & editing, Writing – original draft, Methodology, Conceptualization. **Minghui Zhao:** Writing – review &

editing, Validation, Supervision, Resources, Methodology, Funding acquisition, Data curation. **Xiaobo He:** Writing – review & editing, Validation, Conceptualization. **Jiazheng Zhang:** Writing – review & editing, Software, Investigation. **Jinhui Cheng:** Software, Methodology. **Huabin Mao:** Supervision.

Declaration of competing interest

The authors declare that they have no known competing financial interests or personal relationships that could have appeared to influence the work reported in this paper.

Acknowledgements

The data of this study was supported by the Major Research Plan on West-Pacific Earth System Multispheric Interactions (contracts 91958212), the National Natural Science Foundation of China (contracts 42476059), the Basic and Applied Basic Research Foundation of Guangdong Province (contracts 2024A1515030181), the Special Fund of South China Sea Institute of Oceanology of the Chinese Academy of Sciences (contract SCSIO2023HC08). We are grateful to the crew of the *R/V Shiyan 2* as well as scientists and technicians for their precious involvement during the NORC2015-08 and NORC2016-08 cruises. We strongly thank Walter Mooney for highly improving our manuscript. We are grateful for insightful comments by the Editor Liang Zhao, the reviewer Frauke Klingelhoefer and two other anonymous reviewers, which greatly improved our paper. Some maps are drawn using GMT software (Wessel and Smith, 1995).

Data availability

The data used in this study are available on Zenodo at https://doi.org/10.5281/zenodo.13950561.

References

Amuru, M.L., 2007. Global travel time tomography with 3-D reference models. Geol. Ultraiect. 274, 1–174.

Beyssac, O., Simoes, M., Avouuac, J.-P., Farley, K.A., Chen, Y.-G., Chan, Y.-C., et al., 2007. Late Cenozoic metamorphic evolution and exhumation of Taiwan. Tectonics 26 (TC6001). https://doi.org/10.1029/2006TC002064.

Byrne, T., Chan, Y.C., Rau, R.J., Lu, C.Y., Lee, Y.H., Wang, Y.J., 2011. The arc-continent collision in Taiwan. In: Brown, D., Ryan, P.D. (Eds.), Arc-Continent Collision: New York. Springer, Berlin Heidelberg, pp. 213–245.

Byrne, T., Chojnacki, M., Lewis, J., Lee, J.-C., Ho, G.-R., Yeh, E.-C., et al., 2024. Tectonic exhumation of a metamorphic core in an arc-continent collision during oblique convergence, Taiwan. Progr. Earth Planeta. Sci. 11 (23). https://doi.org/10.1186/s40645-024-00627-w.

Chen, C.L., Yan, P., Yu, J.H., Zhong, G.J., 2023. Seismically imaged crustal breakup in the Southwest Taiwan Basin of the northeastern South China Sea margin. Geochem. Geophys. Geosyst. 24, e2023GC010918. https://doi.org/10.1029/2023GC010918.

Cheng, J.H., Zhang, J.Z., Zhao, M.H., Du, F., Fan, C.Y., Wang, X.Y., et al., 2021. Spatial distribution and origin of the high-velocity lower crust in the northeastern South China Sea. Tectonophysics 819. https://doi.org/10.1016/j.tecto.2021.229086.

Chim, L.K., Yen, J.-Y., Huang, S.Y., Liou, Y.-S., Tsai, L.L.-Y., 2018. Using Raman Spectroscopy of Carbonaceous Materials to track exhumation of an active orogenic belt: an example from Eastern Taiwan. J. Asian Earth Sci. 164, 248–259. https://doi.org/10.1016/j.jseaes.2018.06.030.

Chiu, H., Wang, T.K., Cho, Y.H., 2021. Crustal underplating and overriding across the collision-subduction transition in the northern Manila subduction zone offshore southwestern Taiwan. Mar. Geophys. Res. 42 (22). https://doi.org/10.1007/s11001-021-09444-y.

Christensen, N.I., Mooney, W.D., 1995. Seismic velocity structure and composition of the continental crust: a global view. J. Geophys. Res. Atmos. 100 (B6), 9761–9788. https://doi.org/10.1029/95JB00259.

Dahlen, F.A., 1990. Critical Taper Model of Fold-And-Thrust Belts and Accretionary Wedges. Annu. Rev. Earth Planet. Sci. 18 (1), 55–99. https://doi.org/10.1146/annurev.ea.18.0501900.

Dean, S.M., Minshull, T.A., Whitmarsh, R.B., Louden, K.E., 2000. Deep structure of the ocean-continent transition in the southern Iberia Abyssal Plain from seismic refraction profiles: the IAM-9 transect at 40°20′ N. J. Geophys. Res. 105, 5859–5885. https://doi.org/10.1029/1999JB900301.

Doo, W.-B., Lo, C.-L., Kuo-Chen, H., Brown, D., Hsu, S.-K., 2015. Exhumation of serpentinized peridotite in the northern Manila subduction zone inferred from forward gravity modeling. Geophys. Res. Lett. 42, 7977–7982. https://doi.org/10.1002/2015GL065705.

Doo, W.-B., Kuo-Chen, H., Brown, D., Lo, C.-L., Hsu, S.-K., Huang, Y.-S., 2016. Serpentinization of the fore-arc mantle along the Taiwan arc-continent collision of the northern Manila subduction zone inferred from gravity modeling. Tectonophysics 69, 282–289. https://doi.org/10.1016/j.tecto.2016.10.019.

Du, F., Zhang, J.Z., Yang, F.D., Zhao, M.H., Wang, Q., Qiu, X.L., 2018. Combination of least square and Monte Carlo methods for OBS relocation in 3D seismic survey near Bashi Channel. Mar. Geod. 41 (5), 1–22. https://doi.org/10.1080/01490419.2018.1479993.

Eakin, D.H., Mcintosh, K., Van Avendonk, H.J.A., Lavier, L., Lester, R., Liu, C.-S., et al., 2014. Crustal-scale seismic profiles across the Manila subduction zone: the transition from intraoceanic subduction to incipient collision. J. Geophys. Res. Solid Earth 119 (1), 1–17. https://doi.org/10.1002/2013JB010395.

Fan, C.Y., Xia, S.H., Zhao, F., Sun, J.L., Cao, J.H., Xu, H.L., et al., 2017. New insights into the magmatism in the northern margin of the South China Sea: Spatial features and volume of intraplate seamounts. Geochem. Geophys. Geosyst. 18, 2216–2239. https://doi.org/10.1002/2016GC006792.

Gao, J.W., Wu, S.G., McIntosh, K., Mi, L.J., Yao, B.C., Chen, Z.M., et al., 2015. The continent-ocean transition at the mid-northern margin of the South China Sea. Tectonophysics 654, 1–19. https://doi.org/10.1016/j.tecto.2015.03.003.

Gao, J.W., Wu, S.G., Yao, Y.J., Chen, C.X., Song, T.R., Wang, J.L., et al., 2018. Tectonic deformation and fine structure of the frontal accretionary wedge, northern Manila subduction zone. Chin. J. Geophys. (in Chinese) 61 (7), 2845–2858. https://doi.org/10.6038/cjg2018L0461.

Hamilton, E.L., 1978. Sound velocity-density relations in sea-floor sediments and rocks. J. Acoust. Soc. Am. 63 (2), 366–377. https://doi.org/10.1121/1.381747.

Hsu, S.-K., Yeh, Y.-C., Doo, W.-B., Tsai, C.-H., 2004. New bathymetry and magnetic lineations identifications in the northernmost South China Sea and their tectonic implications. Mar. Geophys. Res. 25, 29–44. https://doi.org/10.1007/s11001-005-0731-7.

Huang, C.-Y., Yuan, P.B., Tsao, S.J., 2006. Temporal and spatial records of active arc-continent collision in Taiwan: a synthesis. Geol. Soc. Am. Bull. 118 (3–4), 274–288. https://doi.org/10.1130/B25527.1.

Kashubin, S.N., Petrov, O.V., Rybalka, A.V., Milshtein, E.D., Shokalsky, S.P., Verba, M.L., et al., 2017. Earth's crust model of the south-Okhotsk basin by wide-angle OBS data. Tectonophysics 710-771, 37–55. https://doi.org/10.1016/j.tecto.2016.11.

Klingelhoefer, F., Berthet, T., Lallemand, S., Schnurle, P., Lee, C.-S., Liu, C.-S., et al., 2012. P-wave velocity structure of the southern Ryukyu margin east of Taiwan: results from the ACTS wide-angle seismic experiment. Tectonophysics 578, 50–62. https://doi.org/10.1016/j.tecto.2011.10.010.

Korenaga, J., Holbrook, W.S., Kent, G.M., Kelemen, P.B., Detrick, R.S., Larsen, H.-C., et al., 2000. Crustal structure of the Southeast Greenland margin from joint refraction and reflection seismic tomography. J. Geophys. Res. 105, 21591–21614. https://doi.org/10.1029/2000JB900188.

Koulakov, I., 2011. High-frequency P and S velocity anomalies in the upper mantle beneath Asia from inversion of worldwide traveltime data. J. Geophys. Res. 116, B04301. https://doi.org/10.1029/2010JB007938.

Lester, R., McIntosh, K., Van Avendonk, H.J.A., Lavier, L., Liu, C.-S., Wang, T.-K., 2013. Crustal accretion in the Manila Trench accretionary wedge at the transition from subduction to mountain-building in Taiwan. Earth Planet. Sci. Lett. 375, 430–440. https://doi.org/10.1016/j.epsl.2013.06.007.

Lester, R., Van Avendonk, H.J.A., McIntosh, K., Lavier, L., Liu, C.-S., Wang, T.K., et al., 2014. Rifting and magmatism in the northeastern South China Sea from wide-angle tomography and seismic reflection imaging. J. Geophys. Res. Solid Earth 119, 2305–2323. https://doi.org/10.1002/2013JB010639.

Li, C., Hilst, R.D., Engdahl, E.R., Burdick, S., 2008. A new global model for P wave speed variations in Earth's mantle. Geochem. Geophys. Geosyst. 9 (5). https://doi.org/10.1029/2007GC001806.

Li, C.F., Sun, Z., Hu, D.K., Wang, Z.W., 2013. Crustal structure and deformation associated with seamount subduction at the North Manila Trench represented by analog and gravity modeling. Mar. Geophys. Res. 34 (3–4), 393–406. https://doi.org/10.1007/s11001-013-9193-5.

Lin, A.T., Watts, A.B., Hesselbo, S.P., 2003. Cenozoic stratigraphy and subsidence history of the South China Sea margin in the Taiwan region. Basin Res. 15 (4), 453–478. https://doi.org/10.1046/j.1365-2117.2003.00215.x.

Liu, Y.T., Li, C.F., Wen, Y.L., Yao, Z.W., Wan, X.L., Qiu, X.L., et al., 2021. Mantle serpentinization beneath a failed rift and post-spreading magmatism in the northeastern South China Sea margin. Geophys. J. Int. 225, 811–828. https://doi.org/10.1093/gji/ggab006.

Liu, S.Q., Gao, J.W., Zhao, M.H., Sibuet, J.-C., 2022. Crustal structure of the northern Manila subduction zone: is thinned continental crust or oceanic crust subducting beneath the Luzon arc and forearc? Tectonophysics 844. https://doi.org/10.1016/j.tecto.2022.229605.

Liu, Y.T., Li, C.F., Qiu, X.L., Zhang, J.Z., 2023. Vp/Vs ratios beneath a hyper-extended failed rift support a magma-poor continental margin in the northeastern South China Sea. Tectonophysics 846, 229652. https://doi.org/10.1016/j.tecto.2022.229652.

Ludwig, W.J., Kumar, N., Houtz, R.E., 1979. Profiler-sonobuoy measurements in the South China Sea basin. J. Geophys. Res. 84 (B7), 3505–3518. https://doi.org/10.1029/JB084iB07p03505.

McIntosh, K., van Avendonk, H.J.A., Lavier, L., Lester, R., Eakin, D., Wu, F., 2013. Inversion of a hyper-extended rifted margin in the southern Central Range of Taiwan. Geology 41 (8), 871–874. https://doi.org/10.1130/g34402.1.

Molli, G., Malavieille, J., 2010. Orogenic processes and the Corsica/Apennines geodynamic evolution: insights from Taiwan. Int. J. Earth Sci. 100, 1207–1224. https://doi.org/10.1007/s00531-010-0598-y.

Nissen, S., Hayes, D., Buhl, P., Diebold, J., Bochu, Y., Weijun, Z., et al., 1995. Deep penetration seismic soundings across the northern margin of the South China Sea. J. Geophys. Res. Solid Earth 1002, 22407–22434. https://doi.org/10.1029/95JB01866.

Pan, C.C., He, X.B., 2023. Subducting passive continental margins with crustal (ultra) mafic intrusions: an underappreciated mechanism for recycling water back into the mantle. Earth Planet. Phys. 7 (1–6). https://doi.org/10.26464/epp2023074.

Qiu, X.L., Ye, S.Y., Wu, S.M., Shi, X.B., Zhou, D., Xia, K.Y., et al., 2001. Crustal structure across the Xisha Trough, northwestern South China Sea. Tectonophysics 341, 179–193. https://doi.org/10.1016/S0040-1951(01)00222-0.

Qiu, X.L., Zhao, M.H., Ao, W., Lu, C.C., Hao, T.Y., You, Q.Y., et al., 2011. OBS survey and crustal structure of the Southwest Sub-basin and Nansha Block, South China Sea. Chin. J. Geophys. (in Chinese) 54 (12), 3117–3128. https://doi.org/10.3969/j.issn.0001-5733.2011.12.012.

Ren, J.Y., Tamaki, K., Li, S.T., Zhang, J.X., 2002. Late Mesozoic and Cenozoic rifting and its dynamic setting in Eastern China and adjacent areas. Tectonophysics 344, 175–205. https://doi.org/10.1016/S0040-1951(01)00271-2.

Ru, K., Pigott, J.D., 1986. Episodic Rifting and Subsidence in the South China Sea. Am. Assoc. Pet. Geol. Bull. 70 (9), 1136–1155. https://doi.org/10.1306/94886A8D-1704-11D7-8645000102C1865D.

Sandwell, D.T., Gracia, E., Soofi, K., Wessel, P., Chandler, M., Smith, W.H.F., 2013. Towards 1 mGal global marine gravity from CryoSat-2, Envisat, and Jason-1. Lead. Edge 32, 892–899. https://doi.org/10.1190/tle32080892.1.

Savva, D., Pubellier, M., Franke, D., Chamot-Rooke, N., Meresse, F., Steuer, S., et al., 2014. Different expressions of rifting on the South China Sea margins. Mar. Pet. Geol. 58, 579–598. https://doi.org/10.1016/j.marpetgeo.2014.05.023.

Sibuet, J.-C., Hsu, S.-K., 2004. How was Taiwan created? Tectonophysics 379 (1–4), 159–181. https://doi.org/10.1016/j.tecto.2003.10.022.

Sibuet, J.-C., Zhao, M.H., Wu, J., Lee, C.S., 2021. Geodynamic and plate kinematic context of South China Sea subduction during Okinawa trough opening and Taiwan orogeny. Tectonophysics 817. https://doi.org/10.1016/j.tecto.2021.229050.

Simoes, M., Beyssac, O., Chen, Y.-G., 2012. Late Cenozoic metamorphism and mountain building in Taiwan: a review. J. Asian Earth Sci. 46, 92–119. https://doi.org/10.1016/j.jseaes.2011.11.009.

Stockwell, J.W., Cohen, J.K., 2002. The New SU user's Manual. Center for Wave Phenomena.

Stolar, D.B., Willett, S.D., Montgomery, D.R., 2007. Characterization of topographic steady state in Taiwan. Earth Planet. Sci. Lett. 261, 421–431. https://doi.org/10.1016/j.epsl.2007.07.045.

Sun, Z., Li, F.C., Lin, J., Sun, L.T., Pan, X., Zheng, J.Y., 2021. The Rifting-Breakup Process of the Passive Continental margin and its Relationship with Magmatism: the Attribution of the South China Sea. Earth Sci. 46 (3), 770–789. https://doi.org/10.3799/dqkx.2020.371.

Tan, P.C., Ding, W.W., Li, J.B., 2022. Exhumation history of the Hengchun Ridge and its implications for Taiwan orogenic processes. Front. Earth Sci. 10, 941040. https://doi.org/10.3389/feart.2022.941040.

Tsai, C.-H., Shyu, J.B., Chung, S.-L., Lee, H.Y., 2019. Miocene sedimentary provenance and paleogeography of the Hengchun Peninsula, southern Taiwan: Implications for tectonic development of the Taiwan orogen. J. Asian Earth Sci. https://doi.org/10.1016/j.jseaes.2019.104032.

Wan, K.Y., Xia, S.H., Cao, J.H., Sun, J.L., Xu, H.L., 2017. Deep seismic structure of the northeastern South China Sea: Origin of a high-velocity layer in the lower crust. J. Geophys. Res. Solid Earth 122, 2831–2858. https://doi.org/10.1002/2016JB013481.

Wan, X.L., Li, C.F., Zhao, M.H., He, E.Y., Liu, S.Q., Qiu, X.L., et al., 2019. Seismic velocity structure of the magnetic quiet zone and continent-ocean boundary in the northeastern South China Sea. J. Geophys. Res. Solid Earth. https://doi.org/10.1029/2019JB017785.

Wang, T.-K., Chen, M.-K., Lee, C.-S., Xia, K.-Y., 2006. Seismic imaging of the transitional crust across the northeastern margin of the South China Sea. Tectonophysics 412, 237–254. https://doi.org/10.1016/j.tecto.2005.10.039.

Wang, K.-L., Lo, Y.-M., Chung, S.-L., Lo, C.-H., Hsu, S.-K., Yang, H.-J., et al., 2012. Age and geochemical features of dredged basalts from Offshore SW Taiwan: the coincidence of intra-plate magmatism with the spreading South China Sea. Terr. Atmos. Ocean. Sci. 23 (6), 657–669. https://doi.org/10.3319/TAO.2012.07.06.01(TT).

Wang, Q., Qiu, X.L., Zhao, M.H., Huang, H.B., Ao, W., 2016. Analysis and processing on abnormal OBS data in the South China Sea. Chin. J. Geophys. (in Chinese) 59 (3), 1102–1112. https://doi.org/10.6038/cjg20160330.

Wang, H.L., Zhao, Q., Huang, J.L., Fan, J.K., 2019. Morphological structure and evolution of accretionary wedge in the northern part of Manila subduction zone. Mar. Sci. 43 (8), 1–16. https://doi.org/10.11759/hykx20181124002.

Wen, Y.L., Li, C.F., Wang, L.J., Liu, Y.T., Peng, X., Yao, Z.W., et al., 2021a. The onset of seafloor spreading at the northeastern continent-ocean boundary of the South China Sea. Mar. Pet. Geol. 133, 105255. https://doi.org/10.1016/j.marpetgeo.2021.105255.

Wen, G.G., Wan, K.Y., Xia, S.H., Fan, C.Y., Cao, J.H., Xu, H.L., 2021b. Crustal extension and magmatism along the northeastern margin of the South China Sea: further insights from shear waves. Tectonophysics 817. https://doi.org/10.1016/j.tecto.2021.229073.

Wessel, P., Smith, W.H.F., 1995. New version of the generic mapping tools released. Eos. Trans. 76, 329.

White, R.S., McKenzie, D., O'Nions, R.K., 1992. Oceanic crustal thickness from seismic measurements and rare earth element inversions. J. Geophys. Res. 97, 19683–19715. https://doi.org/10.1029/92JB01749.

Willett, S.D., Brandon, M.T., 2002. On steady states in mountain belts. Geology 30 (2), 175–178. https://doi.org/10.1130/0091-7613(2002)030<0175:OSSIMB>2.0.CO;2.

Wu, Z.C., Zhang, J.L., Xu, M.J., Li, H.L., 2023. Magnetic anomaly lineations in the Northeastern South China Sea and their implications for initial seafloor spreading. Front. Earth Sci. 10, 1015856. https://doi.org/10.3389/feart.2022.1015856.

Xia, S.H., Zhao, F., Zhao, D.P., Fan, C.Y., Wu, S.G., Mi, L.J., et al., 2018. Crustal plumbing system of post-rift magmatism in the northern margin of South China Sea: New insights from integrated seismology. Tectonophysics 744. https://doi.org/10.1016/j.tecto.2018.07.002.

Xu, S.M., Liu, X., Li, S.Z., Somerville, I., 2022. Subduction-collisional processes between the Eurasian and Philippine Sea plates: Constraints from thermal-age paths of the Taiwan Orogen. Gondwana Res. 102, 385–393. https://doi.org/10.1016/j.gr.2020.07.001.

Yan, P., Zhou, D., Liu, Z.S., 2001. A crustal structure profile across the northern continental margin of the South China Sea. Tectonophysics 338, 1–21. https://doi.org/10.1016/S0040-1951(01)00062-2.

Yao, C.L., Hao, T.Y., Guan, Z.N., Zhang, Y.W., 2003. High-speed computation and efficient storage in 3-D gravity and magnetic inversion based on genetic algorithms. Chin. J. Geophys. (in Chinese) 46, 252–258. https://doi.org/10.1002/cjg2.351.

Zelt, C.A., Forsyth, D.A., 1994. Modeling wide-angle seismic data for crustal structure: Southeastern Grenville Province. J. Geophys. Res. Solid Earth 99, 11687–11704. https://doi.org/10.1029/93JB02764.

Zelt, C.A., Smith, R., 1992. Seismic traveltime inversion for 2-D crustal velocity structure. Geophys. J. Int. 108 (1), 16–34. https://doi.org/10.1111/j.1365-246X.1992.tb00836.x.

Zhang, J.Z., Zhao, M.H., Qiu, X.L., Ruan, A.G., Li, J.B., Chen, Y.S., et al., 2012. OBS seismic data processing and preliminary results on the hydrothermal field of the Southwest Indian Ridge. J. Trop. Oceanogr. 2012 (3), 79–89. https://doi.org/10.3969/j.issn.1009-5470.2012.03.011.

Zhang, J.Z., Qiu, X.L., Zhao, M.H., You, Q.Y., He, E.Y., Wang, Q., 2018. Abnormal data retrieval of three-dimensional OBS survey at the Bashi Channel area of the South China Sea. Chin. J. Geophys. (in Chinese) 61 (4), 1529–1538. https://doi.org/10.6038/cjg2018L0268.

Zhang, H.Y., Qiu, X.L., Zhang, J.Z., He, E.Y., You, Q.Y., 2019. Time record and accurate correction of Chinese OBS raw data. Chin. J. Geophys. (in Chinese) 62 (1), 172–182. https://doi.org/10.6038/cjg2019L0715.

Zhao, M.H., Qiu, X.L., Xia, S.H., Xu, H.L., Wang, P., Wang, T.K., et al., 2010. Seismic structure in the northeastern South China Sea: S-wave velocity and Vp/Vs ratios derived from three-component OBS data. Tectonophysics 480, 183–197. https://doi.org/10.1016/j.tecto.2009.10.004.

Zhao, F., Alves, T., Wu, S.G., Li, W., Huuse, M., Mi, L.J., et al., 2016. Prolonged post-rift magmatism on highly extended crust of divergent continental margins (Baiyun Sag, South China Sea). Earth Planet. Sci. Lett. 445, 79–91. https://doi.org/10.1016/j.epsl.2016.04.001.

Zhu, J.J., Li, S.Z., Sun, Z.X., Li, X.P., Li, J., 2017. Crustal architecture and subduction processes along the Manila Trench, Eastern South China Sea. Earth Science Frontiers 24 (4), 341–351. https://doi.org/10.13745/j.esf.yx.2017-3-13.